



Liquid-diffusion electrode with core-shell structured mixed metal oxide catalyst for near-zero polarization in chlor-alkali electrolysis

Hyun Woo Lim^a, Jae Hyun Park^{a,b}, Bingyi Yan^{a,c}, Jin Young Kim^{a,b,*}, Chan Woo Lee^{d,**}

^a Department of Materials Science and Engineering, Seoul National University, Seoul 08826, Republic of Korea

^b Research Institution of Advanced Materials (RIAM) and Institution of Engineering Research, College of Engineering, Seoul National University, Seoul 08826, Republic of Korea

^c SNU Materials Education/Research Division for Creative Global Leaders, Seoul National University, Seoul 08826, Republic of Korea

^d Department of Chemistry, Kookmin University, Seoul 02707, Republic of Korea

ARTICLE INFO

Keywords:

Liquid-diffusion electrode

Chlorine evolution

Hydrogen evolution

Mixed metal oxide

Chlor-alkali electrolysis

ABSTRACT

Chlor-alkali electrolysis is a key industrial process for the production of chlorine gas, caustic soda, and hydrogen fuels. Here, we demonstrate that a Ti foam electrode, which has a diffusion layer of liquid reactant, deposited with a thin layer of core/shell-structured mixed metal oxide nanoparticles enables almost zero polarization in the range of hundreds of mA cm⁻² towards the chlorine evolution reaction (CER), using noble-metals 20 times lower than commercial electrode. The fast charge-transfer kinetics induce near-zero overpotential at low current densities, while the high mass transport rates aided by porous channels lead to unprecedentedly high CER performance (LSV derived overpotentials of 9 and 44 mV at 10 and 500 mA cm⁻² with Faradaic efficiency of 99.1% and 86.1% in 5.0 M NaCl). Under practical chlor-alkali process conditions, the RNTiO₂/Ti foam exhibited remarkable performance as a bifunctional electrode for CER and hydrogen evolution reaction (HER) with overpotential of 11 mV for HER.

1. Introduction

The chlor-alkali process is a commercial electrochemical reaction that produces chlorine gas, caustic soda, and hydrogen gas via electrolysis of a concentrated sodium chloride solution [1,2]. It consists of two half-reactions: the chlorine evolution reaction (CER) at the anode and the hydrogen evolution reaction (HER) at the cathode, as shown in Eqs. (1) and (2):



Since the development of the process in 1888, the amount of chlorine produced has continuously increased, [2–5] reaching to the annual production of 88 million tons [6,7]. Chlorine derivatives form by hydrolysis of Cl₂ in water, like hypochlorous acid or hypochlorite, are environmentally essential for disinfection and water treatment [8,9]. The used amount of chlorine gas for chlorination accounts for 4.4 million tons every year [10]. Chlorine gas is also used as a raw material

in the manufacture of widely used chemicals and polymers, such as ethylene dichloride, polyvinyl chloride, and polycarbonate [5,11–16]. Furthermore, large amounts of caustic soda and hydrogen energy are generated annually by the chlor-alkali process (96.8 and 2.64 million tons, respectively) [17,18]. Studies on making clean electricity using the chlor-alkali hydrogen by directly integrating fuel cells in electrochemical plants are also underway [19–22].

Dimensionally stable anodes (DSAs), Ti substrates coated with a mixed metal oxide (MMO) film based on precious metals (Ru and Ir) and Ti metal, have been employed as commercial electrocatalysts for the CER. In DSAs, the precious metal oxides are combined with TiO₂, forming a MMO, which is known to improve the durability of the anode [23–25]. Because of their manufacturing advantages, conventional DSAs have been produced by a thermal decomposition method in which painting and heat-treatment (typically 400–550 °C) of the MMO on a Ti plate are repeated 10–12 times [26–28]. As a consequence, DSAs have the form of a two-dimensional dense film composed of sintered particles [28–31]. Owing to such a structural feature, more than 30 at% of precious metals must be put into the film to provide high electrocatalytic

* Corresponding author at: Department of Materials Science and Engineering, Seoul National University, Seoul 08826, Republic of Korea.

** Corresponding author.

E-mail addresses: jkim.mse@snu.ac.kr (J.Y. Kim), cwlee1@kookmin.ac.kr (C.W. Lee).

<https://doi.org/10.1016/j.apcatb.2022.122095>

Received 2 August 2022; Received in revised form 1 October 2022; Accepted 22 October 2022

Available online 25 October 2022

0926-3373/© 2022 Elsevier B.V. All rights reserved.

activity and sufficient electrical conductivity throughout the film [32–34]. This is one of the main problems that needs to be resolved in terms of production cost.

More importantly, another disadvantage of conventional DSAs is that large overpotentials must be applied to the electrode to achieve high current densities of hundreds of mA cm^{-2} , in spite of the large amount of noble metals. For example, previous reports show that DSAs require 40–60 mV of overpotential at 10 mA cm^{-2} in over 3.5 M NaCl at 25°C , whereas approximately 80, 110, and more than 320 mV are needed to drive 50, 100, and 300 mA cm^{-2} , respectively, representing significant increases in the overpotential [35–39]. These results indicate that the CER requires large overpotentials at high current densities, although the overpotential at the onset potential can be quite low [25,40–44].

According to the extended Butler–Volmer model, which describes the fundamental relationship between current density and overpotential over a two-dimensional electrode surface, the current density highly depends on the reactant and product concentrations at the electrode surface [45,46]. Moreover, the equation shows that accelerating the rates at which reactants are supplied and products are removed around the electrode surface by mass transport processes, such as diffusion, convection, and migration, is critically important for reducing the overpotential, especially at a high current density.

Gas-diffusion electrodes (GDEs) have been used to improve the current density to several orders of magnitude higher in many electrochemical applications, including fuel cells and carbon dioxide reduction. GDEs are typically constructed by stacking a gas-diffusion layer (GDL) and a catalyst layer, where gaseous reactants can be supplied to the catalyst layer through the porous GDL from the back surface of the electrode, and are preserved at a high concentration in the vicinity of the catalyst [47]. In a similar context, inspired by the GDE, it is conceivable that liquid reactants for the CER like the hydrated chlorine ions can be injected into the electrode through porous channels that supply an aqueous electrolyte across the electrode. Such a three-dimensional porous electrode can facilitate much faster diffusion of liquids. Furthermore, using an electrically conductive porous scaffold deposited with a thin catalyst layer can provide pathways for electron conduction, while minimizing the use of noble metals.

Here, we report a liquid-diffusion electrode (LDE) that enables near-zero polarization for the CER even at a high current density of 500 mA cm^{-2} . The electrode was fabricated by depositing mixed-oxide nanoparticles of major Ru, Ti, and minor Nb elements on porous Ti foam (abbreviated as RNTO/Ti foam). More specifically, the active site for the CER possesses a core/shell structure in which the mixed-oxide nanoparticles of Ru–Ti–Nb oxide are passivated with a thin TiO_2 shell, resulting in durable performance at a high current density. The RNTO/Ti foam showed a very low charge transfer resistance (R_{ct}) and diffusion resistance (R_{d}) compared to those of the control samples, RNTO/Ti foil, and commercial DSA, owing to the large electrochemically active surface area, high electrical conduction, and channels for fast mass transport. The RNTO/Ti foam exhibited a LSV derived overpotential of 9 mV at 10 mA cm^{-2} , with a high Faradaic efficiency (FE) of 99.1% in 5.0 M NaCl ($\text{pH} = 2$) and maintained a low overpotential of 44 mV up to a high current density of 500 mA cm^{-2} , which is a record-high performance among reported studies for the CER. The RNTO/Ti foam also showed durable performance with negligible degradation during long-term electrolysis for 24 h at a high current density of 400 mA cm^{-2} . Furthermore, the RNTO/Ti foam was also evaluated for use in the chlor-alkali process under practical electrolysis conditions: the anolyte and catholyte were saturated NaCl and 3.0 M NaOH/3.0 M NaCl at 90°C , respectively. Remarkably, the RNTO/Ti foam showed excellent performance for the CER, as well as the HER, with low overpotentials of 64 and 63 mV, respectively, at a high current density of 100 mA cm^{-2} . A chlor-alkali electrolyzer equipped with a cathode and anode of the RNTO/Ti foams ultimately allowed for cell operation at approximately 1.84 V and 100 mA cm^{-2} .

2. Experimental sections

2.1. Synthesis of RNTO/Ti foam

RNTO/Ti foam was synthesized in the order of oxidation, hydrothermal method, and then thermal annealing at low temperature under air. The oxidation was proceeded by immersing the Ti foam (MTI-KOREA, EQ-TiF-1106, porosity: 40%) into H_2O_2 solution (Aldrich, 50 wt %) at 70°C for 30 min. Nb-doping of Ti foam with a thin titania layer via oxidation was performed by hydrothermal method at 180°C for 6 h (at a heating rate of $10^\circ\text{C min}^{-1}$) using a solution of 0.001 M NbCl_5 (Aldrich, 99%). After drying overnight in a vacuum oven at 70°C , the deposition of Ru-based particles was also performed by hydrothermal method at 150°C for 10 h using a 0.016 M $\text{RuCl}_3 \cdot 3 \text{H}_2\text{O}$ (Aldrich 99.98%) solution. The deionized water used to make solution was generated using Human Corporation, Model Human RO 180. All hydrothermal processes were performed using a 100 mL Teflon-lined autoclave. In order to prevent homogeneously synthesized particles from falling on the electrode and sticking to the electrode, the glass substrate was fixed as a roof above the Ti foam electrode in hydrothermal processes as depicted in Fig. S1.

2.2. Materials characterization

The morphologies and porosity ratio of the electrodes were characterized by field-emission scanning electron microscopy (FESEM) (Model SU70, Hitachi) at an acceleration voltage of 15 kV. The magnified morphologies of the electrodes, elemental mapping, and selected-area electron diffraction (SAED) pattern are obtained using transmission electron microscopy (TEM) (Model JEM-2100 F, JEOL Ltd.) at an acceleration voltage of 200 kV. The line scan profile and elemental mapping of the catalysts was performed using spherical aberration (Cs)-corrected monochromated TEM (Themis Z, Thermo Fisher) at an acceleration voltage of 300 kV. The X-ray diffraction (XRD) (Model D8 Advance.2020, Bruker) with $\text{Cu K}\alpha$ radiation ($\lambda = 0.1542 \text{ nm}$) was carried out to measure the crystallinity and crystal orientation of the structure. The amount of dissolved elements in the electrolyte was measured using inductively coupled plasma-mass spectrometry (ICP-MS).

2.3. Electrochemical cell construction

A three-electrode system was constructed using catalyst electrode, Pt wire (CE-1, NEO Science), and an Ag/AgCl electrode (Model MF-2052, BASi) as the working electrode, counter electrode, and reference electrode, respectively (Fig. S2a). H-type cell separating working electrode and counter electrode using Nafion membrane (NR212, Ion Exchange Materials) was used. Before attached between working electrode cell and counter electrode cell, Nafion membrane was pre-treated with H_2O_2 and 0.5 M H_2SO_4 (Aldrich, 0.25 M) and washed with deionized water for each step. All pre-treatment and washing process was performed at 70°C for 1 h. A two-electrode system was constructed in the same order as the three-electrode system, except for the reference electrode (Fig. S2b). In order to refresh the electrolyte in the H-type cell, a digital peristaltic pump (EMP-600A, SCIST) was used to circulate the electrolyte between the bulk and the cell.

2.4. Electrochemical measurements

Electrochemical measurements except for electrochemical impedance spectroscopy (EIS) were performed on a potentiostat (Model PARSTAT MC, Princeton Applied Research, USA). All potentials were first IR compensated as the following equation:

$$E_{\text{compensated}} = E_{\text{measured}} - IR_s \quad (1)$$

where, $E_{\text{compensated}}$, E_{measured} , and R_s represent IR-compensated

potential, experimentally measured potential and solution resistance. And then IR compensated potential is converted into the reversible hydrogen electrode (RHE) reference scale with the following equation:

$$E_{\text{RHE}} = E_{\text{Ag/AgCl}} + 0.197\text{V} + \left(\frac{RT \ln 10}{F}\right) \text{pH vs. RHE} \quad (2)$$

where R , T , and F represent the gas constant ($8.314 \text{ J K}^{-1} \text{ mol}^{-1}$), the temperature (in Kelvin), and the Faraday constant ($96,485.3 \text{ C mol}^{-1}$). The linear sweep voltammetry (LSV) scans were measured from 0.4 to 1.5 V vs Ag/AgCl in 5.0 M NaCl (pH = 2) at a scan rate of 10 mV s^{-1} . All current densities were normalized to a geometric area of 1 cm^2 . In order to compare the performance by measuring overpotentials, we calculated the equilibrium potential of CER using the equation reported:

$$E_{\text{CER}}(T, \alpha(\text{Cl}^-), \alpha(\text{Cl}_2)) = E_{\text{CER}}^0(T) - \frac{RT}{F} \ln \alpha(\text{Cl}^-) + \frac{RT}{2F} \ln \alpha(\text{Cl}_2) \quad (3)$$

where $\alpha(\text{Cl}^-)$ to be 0.01 assumed by Guerrini et al. and is related to the partial pressure of Cl_2 that occurs under Ar purging, [48] and $\alpha(\text{Cl}_2)$ was determined depending on the molar concentration of the electrolyte [41]. The standard reduction potential (E_{CER}^0) of CER, which is sensitive to temperature, was derived through the following equation:

$$E_{\text{CER}}^0 = \left[1.358\text{V} + \left(\frac{RT \ln 10}{F}\right) \text{pH} \right] - \left(\frac{dE^0}{dT}\right) \times (T - 298.15\text{K}) \quad (4)$$

where $\frac{dE^0}{dT}$ is equal to 0.001248, according to previous reports [44,49]. The overpotential is calculated by subtracting the experimentally measured potential required to obtain a specific current density from the equivalent potential. The calculated overpotentials are plotted along with the logarithm of the current density ($\log|j|$) to obtain a Tafel plot according to the following equation:

$$\eta = A \log\left(\frac{j}{j_0}\right) \quad (5)$$

where, η , A , and j_0 represent the overpotential, Tafel slope, and the exchange current density. The FE was measured using DPD colorimetry (*N,N*-diethyl-*p*-phenylenediamine) using a pocket colorimeter II (Hach) after the chronoamperometry for 3 min at different current densities generating chlorine species. After the electrolyte obtained by chronoamperometry was diluted 10 times, the reagent was reacted with chlorine species in the electrolyte to make the electrolyte transparent pink, and the molar concentration of chlorine species was quantified from the difference in absorbance with a pocket colorimeter II. Finally, the FE was calculated using the following equation:

$$\text{FE} = \frac{2 \times [\text{Cl}_{2,\text{DPD}}] \times F}{i \times t} \quad (6)$$

where, $[\text{Cl}_{2,\text{DPD}}]$, i , and t represent the molar concentration of the chlorine species, applied current, and electrolysis time [7,50,51]. The Ru wt% for normalizing the current densities of the RNT0/Ti foam and DSA was determined using ICP-MS. The weight and size of the samples for ICP-MS were measured and normalized to a geometric area of 1 cm^2 , and the Ru mass was calculated using the sample weight and wt%. The electrochemically active surface area (ECSA) was calculated using double-layer capacitances (C_{dl}) obtained by cyclic voltammetry (CV) in a non-faradaic potential range of 0.0–1.3 V vs. RHE at different scan rates in 5.0 M NaCl (pH = 2) [52]. The Ti foil was assumed to be flat and used as a control. For example, the geometric electrode area of 0.5 cm^2 for Ti foil was set to be equal to the ECSA value of 0.5 cm^2 . The ECSA value for Ti foil was $6.2 \times 10^{-3} \text{ mF cm}^{-2}$. EIS were performed using a potentiostat (Model Zennium, Zahner-Elektrik) with an AC voltage of 20 mV to measure the electrodes in the frequency range of 10 mHz to 20 kHz in 5.0 M NaCl (pH = 2). The E_{CER} (1.38 V vs. RHE) was applied to evaluate the ohmic resistance (R_{Ω}), R_s , charge transport resistance

(R_{tms}) and R_{ct} , and the potential 50 mV higher than the E_{CER} (1.43 V vs. RHE) was applied to measure the R_{Ω} . The R_{tms} , R_{ct} , and R_{d} of the electrodes were evaluated in the frequency ranges of 20–10 kHz, 10 kHz to 10 Hz, and 10 Hz to 10mHz [53,54]. In order to compare the R_{d} according to the convection rate, in the measurement where a potential of 1.43 V vs. RHE was applied, the rpm was increased (0, 250, 500, 750 rpm). The results of EIS were fitted using Zview. The practical chlor-alkali electrolysis was first performed in the three-electrode. The saturated NaCl (pH = 6) was used as the anolyte and 3.0 M NaOH + 3.0 M NaCl (pH = 14.4) was chosen as the catholyte and both electrolytes were heated to 90°C . The overpotential of the CER was obtained by calculating the E_{CER} using Eqs. (2) and (3). In the case of HER, the equilibrium potential of HER (E_{HER}) was calculated using the following equation:

$$E_{\text{H}^+/\text{H}_2} = E_{\text{H}^+/\text{H}_2}^0 + \left(\frac{RT}{F}\right) \log\left(\frac{a_{\text{H}^+}}{P_{\text{H}_2}^{-1/2}}\right) \quad (7)$$

where, $E_{\text{H}^+/\text{H}_2}^0$ is a constant conditionally equal to 0 at all temperatures and 1 atm of hydrogen pressure, a_{H^+} the activity of hydrogen ion, and $P_{\text{H}_2}^{-1/2}$ the pressure of hydrogen gas [55]. The overpotential of HER was also calculated by the potential difference between the measured potential and the $E_{\text{H}^+/\text{H}_2}$ (E_{HER}). The two-electrode system measurement was performed using the prepared two-electrode cell before. The saturated NaCl and 3.0 M NaOH/3.0 M NaCl were also used for anolyte and catholyte. The electrolytes were also heated to 90°C and refilled using a home-made flow cell to refresh the reactants that were rapidly consumed at high temperatures. The equilibrium cell potential was calculated by adding E_{CER} and E_{HER} under measurement condition. In the chrono-potentiometric curve at 100 mA cm^{-2} , the geometric area of the electrode was adjusted to 0.25 cm^2 in order to reduce the increase in membrane resistance due to the failure of the passage of electric charges generated in the electrode and accumulated in the membrane.

3. Results and discussion

3.1. Synthesis and characterization of RNT0/Ti foam

The RNT0/Ti foam was prepared by treating porous Ti-foam electrodes using a series of facile wet-chemical methods: chemical oxidation and hydrothermal methods, followed by thermal annealing. The Ti foam was first immersed in a H_2O_2 solution to form a thin titania layer on the metal surface of the foam [56]. A thin titania layer can act as a conductive catalyst support by Nb doping, for the loading of RuO_2 nanoparticles, which are the catalytic active sites [7,50]. Furthermore, this layer supplies Ti atoms to the loaded RuO_2 to form a mixed oxide during air-annealing. As shown in the scanning electron microscopy (SEM) images of the pristine Ti foam and Ti foam oxidized by hydrogen peroxide (Fig. S3), oxidation led to the growth of a sponge-like rough oxide layer on the flat Ti surface. The thickness of the oxide layer was measured to be approximately 39.2 nm from the depth profile analysis using X-ray photoelectron spectroscopy (XPS) (Fig. S4).

The oxidized Ti foam was doped with Nb via a hydrothermal method. It has been reported in our previous studies that Nb doping enhances the electrical conductivity of titania and enables thermal diffusion of the Ti atoms at low temperatures [7]. RuO_2 nanoparticles were then deposited by a hydrothermal method. Finally, the prepared sample was annealed at 200°C to drive interatomic diffusion and promote the formation of a mixed oxide. The RNT0/Ti foam is depicted schematically in Fig. 1a, with its structural features, porous properties, and catalytic active sites, which are discussed in detail in the following paragraphs.

The microstructure of the RNT0/Ti foam was analyzed by obtaining back scattered electron (BSE) images from a SEM instrument. BSE analysis is sensitive to z-contrast, which clearly shows the borderlines between the pores and Ti structures at a high depth resolution. As seen in

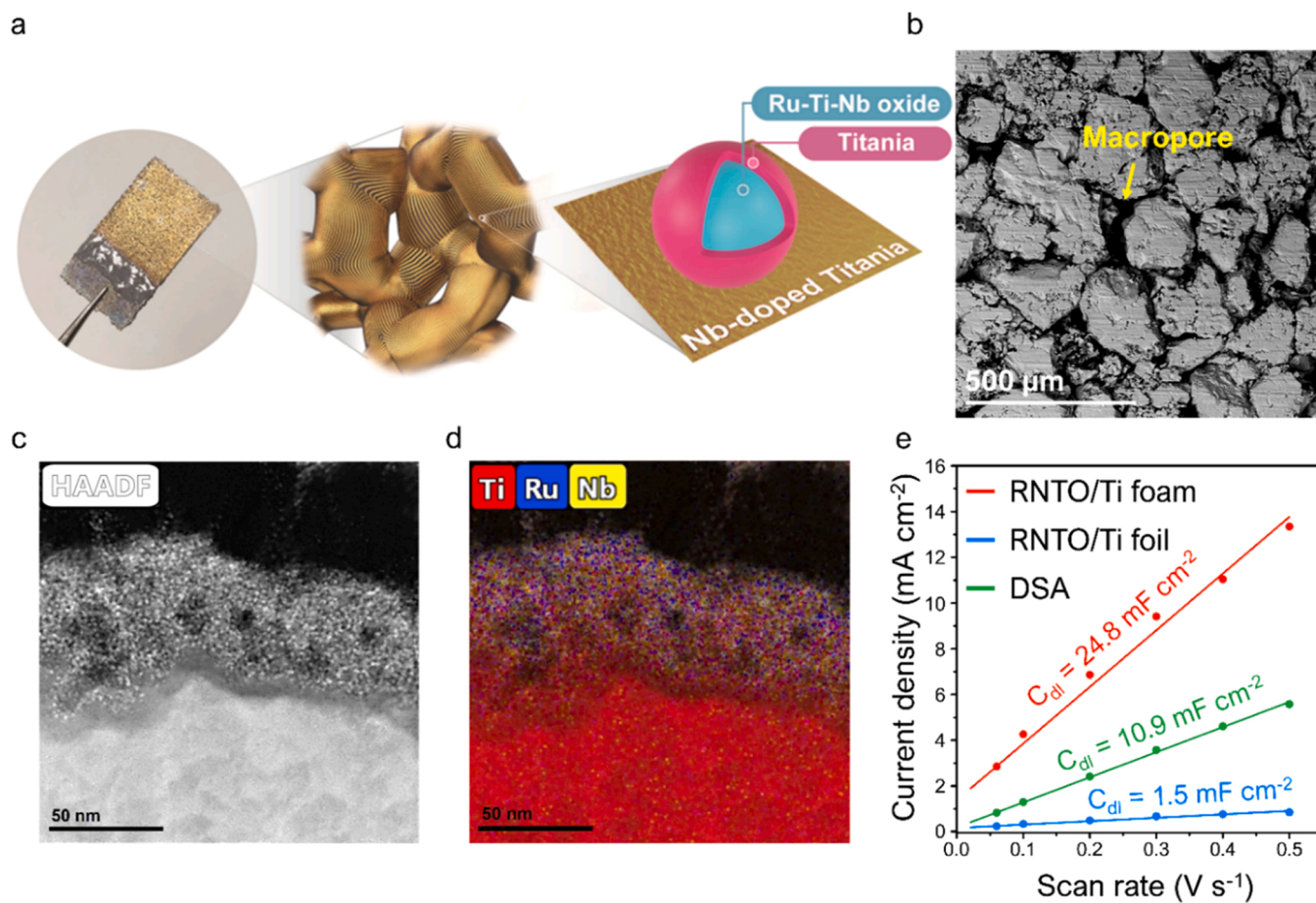


Fig. 1. (a) Schematic illustration of the RNTO/Ti foam electrocatalysts. (b) BSE image of RNTO/Ti foam. (c) and (d) HAADF-STEM image and elemental mapping of RNTO/Ti foam, respectively. (e) Linear fitting of capacitive current densities of RNTO/Ti foam, RNTO/Ti foil, and DSA vs. scan rate.

Fig. 1b, macropores, which are defined as having a pore size larger than 50 nm, are sparsely distributed between the Ti structures. We evaluated the porosity of the RNTO/Ti foam based on SEM analysis (Fig. S5), which was approximately 38.7%, similar to the reported porosity of the pristine Ti foam used in this study. Mesopores with pore sizes between 2 and 50 nm were also detected in the high-magnification SEM images (Fig. S6). The H₂O₂ oxidation process helped create many mesopores across the catalyst layer via surface roughening.

The cross-sectional image of the RNTO/Ti foam electrode was investigated by the high-angle annular dark-field scanning transmission electron microscopy (HAADF-STEM) analysis (Fig. 1c and d). The results showed that a porous nanoparticle layer of mixed oxide composed of Ru, Nb, and Ti (approximately 40 nm in thickness) was formed above the compact Ti layer of the foam. Elemental mapping analysis showed that the average elemental compositions of Ti, Ru, and Nb were 70.4%, 9.5%, and 20.1%, respectively (Fig. S7), indicating that Ru and Nb were well-incorporated into the grown titania layer.

The ECSA of the RNTO/Ti foam was further investigated to evaluate the number of catalytically active sites of the macro/mesoporous foam electrode (Fig. 1e). The ECSA was measured using the double-layer capacitance (C_{dl}) method by cyclic voltammetry scans of the samples in the potential range between 0.0 and 1.3 V at different scan rates (Fig. S8). The C_{dl} value of the RNTO/Ti foam was calculated to be 24.8 mF cm⁻², which is 2.3 and 16.5 times higher than that of the DSA (10.9 mF cm⁻²) and RNTO/Ti foil (1.5 mF cm⁻²) control samples, respectively. The RNTO/Ti foil was prepared using the same procedure as the RNTO/Ti foam, but a two-dimensional Ti foil was used as the substrate.

To investigate the nanostructure and crystallographic properties of the catalyst layer in the RNTO/Ti foam electrode, we performed Cs-

corrected HAADF-STEM analysis at high resolution, as shown in Fig. 2a. The z-contrast image separates the regions where the light element Ti (Z = 22) and the heavy elements Ru (Z = 44) and Nb (Z = 41) are dominant. The crystal structure of the bright nanoparticles was analyzed by measuring the d-spacing, which was assigned to the (101) plane of rutile RuO₂ (JCPDS no. 40-1290). In contrast, the d-spacing of the darker regions was indexed to the (101) plane of anatase TiO₂ (JCPDS no. 21-1272). These results indicated that Ru-dominant oxide nanoparticles of the rutile phase were deposited on the support of the Ti-dominant anatase. Diffraction spots corresponding to the rutile and anatase phases were also clearly observed in the SAED pattern analysis (Fig. S9). XPS analysis was additionally performed to investigate the valency state of metal elements (Fig. S10). In the core-level spectrum of Ru composed of C 1s and Ru 3d, the Ru 3d_{5/2} peak at 280.7 eV can be assigned to RuO₂ (Ru⁴⁺) [57,58]. The Ti 2p_{3/2} and Nb 3d_{5/2} peaks at 458.6 and 207.5 eV correspond to the oxides of Ti⁴⁺ and Nb⁵⁺, respectively, based on previous studies [58,59]. XRD analysis showed diffraction peaks of Ti metal, but other diffractions from the mixed oxide layer were not clearly detected, possibly because of the relatively low crystallinity and peak broadening (Fig. S11).

Detailed elemental mapping results (Fig. 2b and S12) were obtained for the rutile and anatase phases using HAADF-STEM EDS analysis to quantitatively investigate the composition and nanostructure of the active sites. For the rutile nanoparticles, the atomic percentages were measured to be 52.7 at% Ti, 38.5 at% Ru, and 8.8 at% Nb (Fig. 2b), whereas the anatase support showed 72.2 at% Ti, 7.6 at% Ru, and 20.2 at% Nb (Fig. S12). In addition, the line-scan profile was recorded to evaluate the spatial distribution of the elements in the rutile region (Fig. 2c). It was confirmed that a mixed oxide surrounded by an ultrathin

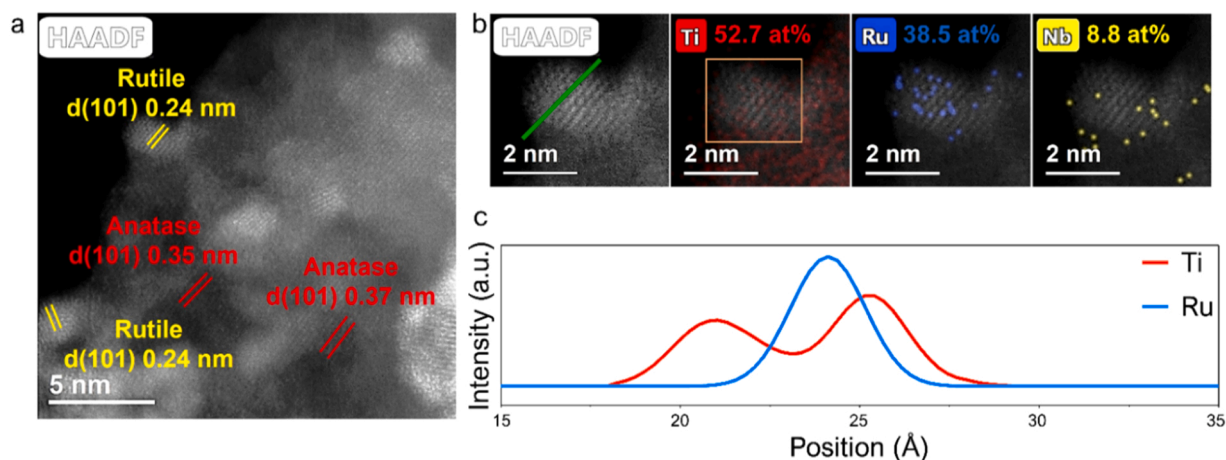


Fig. 2. (a) HAADF-STEM image of RNTiO/Ti foam. (b) and (c) Elemental mapping images and line-scan profiles of RNTiO/Ti foam obtained through HAADF-TEM EDS analysis. The proportions of the elements were obtained from the orange square shown in Fig. 2b.

titania layer was formed by interatomic diffusion. The Fig. S13 also shows that the nanoparticle is surrounded by TiO_2 in several directions. Furthermore, in the HAADF-STEM image, the core-shell nanoparticle shows z-contrast between Ti and Ru elements near the surface. The bright core composed of Ru and Ti is surrounded by the darker layer of Ti. In summary, these results indicated that Ru-rich Ru-Ti-Nb oxide nanoparticles of the rutile phase with a particle size of approximately 2 nm were well synthesized onto the Ti-rich Ti-Ru-Nb oxide support with an anatase phase. More importantly, it was identified that the Ru-

rich nanoparticles had a core/shell structure where the mixed-oxide core was enclosed by an electrochemically durable titania shell, which was expected to improve the stability of the synthesized catalyst under harsh electrochemical conditions, based on the Pourbaix diagram and a previous report [7,60].

3.2. Electrocatalytic performance for CER

The electrocatalytic activities of the RNTiO/Ti foam, RNTiO/Ti foil,

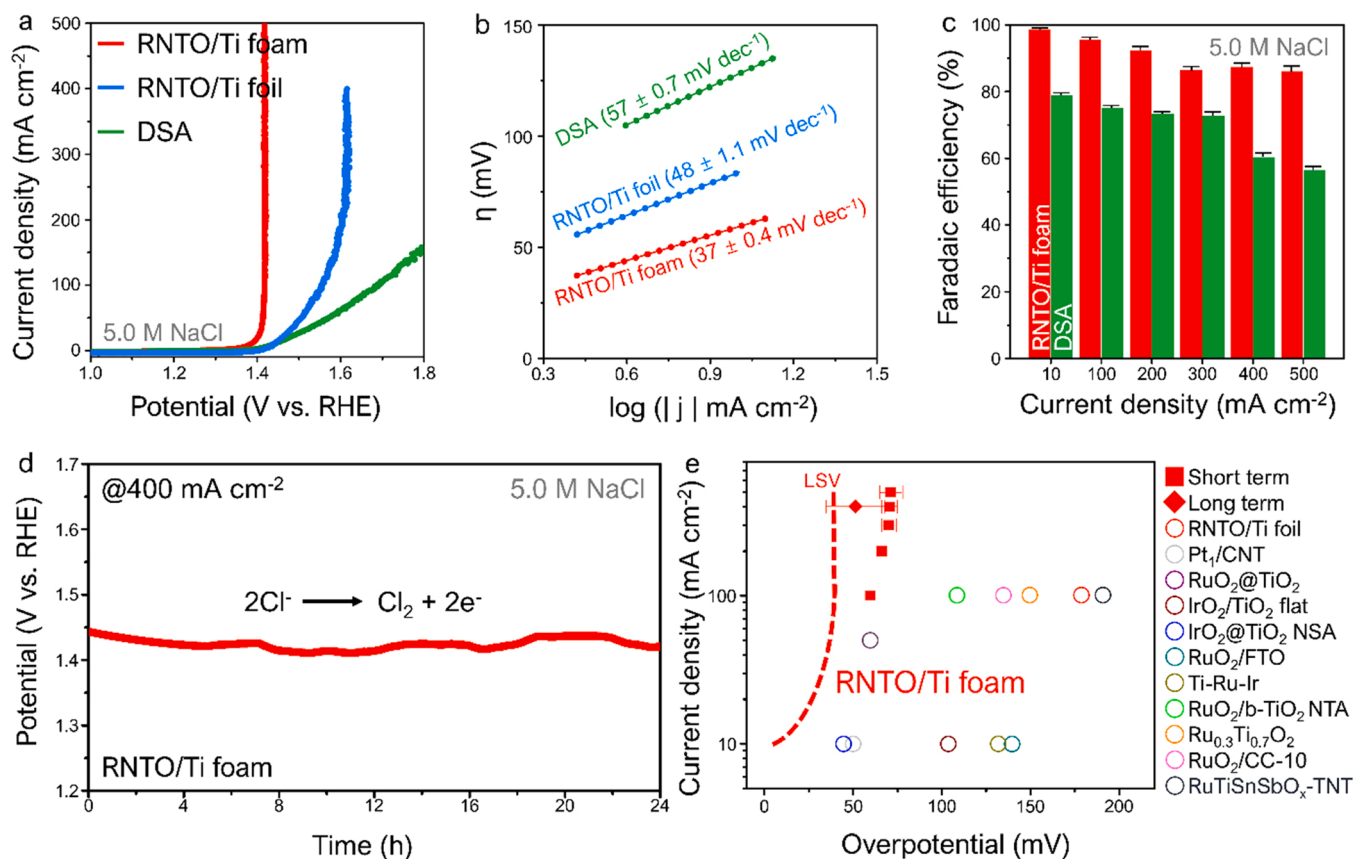


Fig. 3. (a) LSV curves of RNTiO/Ti foam, RNTiO/Ti foil, and DSA measured at a scan rate of 10 mV s^{-1} in 5.0 M NaCl electrolyte (pH = 2). (b) Tafel plots of RNTiO/Ti foam, RNTiO/Ti foil, and DSA. (c) FEs of RNTiO/Ti foam and DSA obtained through electrolysis of 3 min at 10, 100, 200, 300, 400, and 500 mA cm^{-2} . (d) Chronopotentiometry curve of the RNTiO/Ti foam at a fixed current density of 400 mA cm^{-2} for 24 h (electrolyte was continuously supplied using a home-made flow cell). (e) Comparison of CER performance with those of reported catalysts. Details of the measurements are described in the ESI.

and DSA for the CER were evaluated by linear sweep voltammetry (LSV) with a magnetic stirring rate of 500 rpm at 10 mV s^{-1} in 5.0 M NaCl (pH = 2) (Fig. 3a). The LSV scans for all samples were performed repeatedly until the 50th scan, and the LSV data show the current density-potential curve recorded at the final scan. The overpotential of the RNTO/Ti foam derived from LSV was only 9 mV at 10 mA cm^{-2} ($E_{\text{CER}} = 1.38 \text{ V}$ vs. RHE at 25°C in 5.0 M NaCl (pH = 2)), whereas the overpotential values for the RNTO/Ti foil and DSA were 66 and 65 mV, respectively. These results indicate that the active sites of the RNTO/Ti foam exhibited fast CER kinetics. More importantly, even at high current densities of $400 - 500 \text{ mA cm}^{-2}$, the RNTO/Ti foam showed a very low overpotential of only 44 mV, with a steep increase in the current density. In comparison, the RNTO/Ti foil exhibited a 200 mV higher overpotential at the same current density. In addition, the plot of ECSA-normalized current density showed that the overpotential of RNTO/Ti foam is 75 and 350 mV lower than those of RNTO/Ti foil and DSA, respectively, at $0.8 \text{ mA cm}^{-2}_{\text{ECSA}}$ (Fig. S14). These results indicate that the three-dimensional porous structure of the RNTO/Ti foam electrode is a critical factor that allows for an efficient CER at high current densities.

Tafel analyses were performed to investigate the reaction mechanism of the electrocatalysts in the CER (Fig. 3b). The RNTO/Ti foam exhibited a remarkably low Tafel slope of 37 mV dec^{-1} in the overpotential range of 0–60 mV. The Tafel slope of 37 mV dec^{-1} was close to the theoretical value of 40 mV dec^{-1} , indicating that the CER operated with the Volmer–Heyrovsky mechanism over the RNTO/Ti foam, and the second electron transfer to an adsorbed Cl intermediate is the rate-determining step [61–64]. In contrast, the Tafel slopes for the RNTO/Ti foil and DSA were measured to be 48 and 57 mV dec^{-1} , respectively, showing that a higher overpotential was needed to increase the current density by an order of magnitude. The exchange current density (j_0) was estimated from the intercept of the Tafel plots and can be correlated with the charge-transfer resistance through the equation $R_{\text{ct}} = RT/Fj_0$, where R is the gas constant and F is the Faraday constant, which helps in evaluating the charge-transfer kinetics of the electrocatalysts. The j_0 value of the RNTO/Ti foam was $0.42 \pm 0.004 \text{ mA cm}^{-2}$, representing faster charge-transfer kinetics compared to the other samples (0.35 ± 0.01 and $0.21 \pm 0.003 \text{ mA cm}^{-2}$ for the RNTO/Ti foil and DSA, respectively).

The FE of the RNTO/Ti foam for the CER was investigated to quantitatively determine the amount of charge used for the CER and to confirm the CER–oxygen evolution reaction (OER) selectivity (Fig. 3c). The OER is a major competing reaction. The product analysis for CER was conducted using the DPD colorimetric method after bulk electrolysis at various potentials. Fig. S15 shows the potential vs time curve and the average overpotential values recorded at various current densities. The detailed procedure for the FE measurements can be found in the Experimental section (see ESI). The RNTO/Ti foam exhibited an exceptional FE of 99.1% for chlorine generation at 10 mA cm^{-2} and FEs greater than 85% at high current densities (99.1%, 95.7%, 92.3%, 86.5%, and 86.1% at 10, 100, 200, 300, 400, and 500 mA cm^{-2} , respectively). In contrast, the DSA, a control sample, showed 88.7%, 75.1%, 73.5%, 72.9%, 60.4%, and 56.6% at 10, 100, 200, 300, 400, and 500 mA cm^{-2} , respectively. In comparison with the DSA, the RNTO/Ti foam exhibited superior FEs by 20% or more on average at different current densities. Furthermore, we identified from ICP-MS analysis (Fig. S16) that the amount of noble metals can be lowered by 20 times in the RNTO/Ti foam ($0.00015 \text{ g}_{\text{Ru}} \text{ cm}^{-2}$) than in DSA ($0.003 \text{ g}_{\text{Ru}} \text{ cm}^{-2}$). The current density-potential plot normalized by Ru mass (Fig. S17) shows that the RNTO/Ti foam is energy-efficient as well as cost-effective.

Chronopotentiometry was performed to examine the stability of the RNTO/Ti foam at 400 mA cm^{-2} (Fig. 3d). The RNTO/Ti foam maintained a potential near 1.44 V vs. RHE during 24 h of CER operation in 5.0 M NaCl with a fluctuation of 33 mV. In addition, the FE was measured every 4 h to investigate the degradation in the CER performance during the durability test. The RNTO/Ti foam retained an FE of approximately 95% (Fig. S18). Moreover, it was identified by ICP-MS

analysis that Ru was not detected in the electrolyte after chronopotentiometry experiments (Table S1). The HAADF-STEM image of RNTO/Ti foam taken after electrolysis also showed that the titania layer was maintained well without deformation (Fig. S19). These results indicate that RuO_2 corrosion ($\text{RuO}_2 + 2\text{H}_2\text{O} \rightarrow \text{RuO}_{4(\text{aq})} + 4\text{H}^+ + 4\text{e}^-$), a major catalyst degradation mechanism, [65,66] is successfully suppressed in the RNTO/Ti foam even under harsh electrolysis conditions, due to the passivating titania layer [7,40].

For comparison, the catalytic performances of the previously reported electrocatalysts for the CER are plotted in Fig. 3e in terms of current density and overpotential, based on the database of Table S2, where the catalyst materials, overpotential, current density, FE, electrolyte, and operation temperature for previous studies on various types of DSAs and other CER catalysts are listed with relevant references [7, 35–37, 50, 67–73]. The overpotential values were calculated based on the Nernst equation. The RNTO/Ti foam exhibited the best performance among the reported catalysts, with LSV derived overpotentials of 9, 42, and 44 mV at 10, 100, and 500 mA cm^{-2} , respectively. In addition, the overpotential values obtained from short and long bulk electrolysis are also shown in Fig. 3e. In particular, we demonstrated for the first time that a CER can operate with almost zero overpotential at a low current density. Furthermore, at an extremely high current density of 500 mA cm^{-2} , such a low overpotential has never been achieved. This suggests that the RNTO/Ti foam is an attractive candidate for practical CER applications.

To understand the activity origin of the core/shell structured catalyst, we tried to modify the structure of the active site by changing the annealing time at 200°C . The annealing process not only causes the formation of mixed metal oxide via thermal atomic diffusion, but also involves the growth of titania shell. Therefore, it was assumed that controlling annealing time affects the composition of core material as well as the shell thickness. The HAADF-STEM EDS line-scan analyses were performed to identify the structural variation of samples (Fig. 4a and S20). The EDS line scan profile in the Fig. 4a is a representative data for each sample. Other line scan results and HAADF-STEM images are also shown in Fig. S20. Since the data was recorded within a short time to avoid sample drift in the high-magnification, the signal intensity was not sufficient and not continuous with respect to the position. Nevertheless, based on several line scan data (Fig. S20), it was able to observe the evolution trend of elemental distribution and the change in the thickness of TiO_2 shells. Without annealing, the active site existed as just RuO_2 rather than mixed oxide (Fig. 4a-A). However, after annealing at 200°C for 15 min, the MMO was partly formed (Fig. 4a-B). As the annealing duration is prolonged up to 1 h, the complete formation of MMO was observed (Fig. 4a-C). And then, the titania shell became thicker from 0.47 to 1.17 nm by longer heat treatment from 1 h to 8 h (Fig. 4a-D). These analysis results represent that annealing time is a key variable for engineering of composition and structure of active site.

The electrocatalytic activity of RNTO/Ti foam samples prepared with different annealing conditions was evaluated by performing consecutive LSV scans at a rate of 10 mV s^{-1} in 5.0 M NaCl electrolyte at pH 2 (Fig. 4b). The LSV curves measured at the 10th, 20th, 30th, 40th, and 50th cycles were plotted. As the number of cycle increases, the curves get gradually transparent. The CER performance was significantly varied with different annealing time. As shown in Fig. 4b, without annealing and with a short annealing treatment for 15 min, the electrocatalytic activity was considerably low and the current density was not stable in consecutive LSV scans. In contrast, the samples that are thermally treated for 1 h and 8 h showed stable and much higher electrocatalytic activity. However, too long annealing led to a significant decrease in the CER performance. In specific, for the 10th cycle, the overpotential at 100 mA cm^{-2} was 424, 120, 115, and 42 mV for the samples treated for 0 min, 15 min, 1 h, and 8 h. For the 50th cycle, the overpotential value was recorded to be 544, 154, 114, and 42 mV, respectively. Taken together, based on the HAADF-STEM EDS analysis

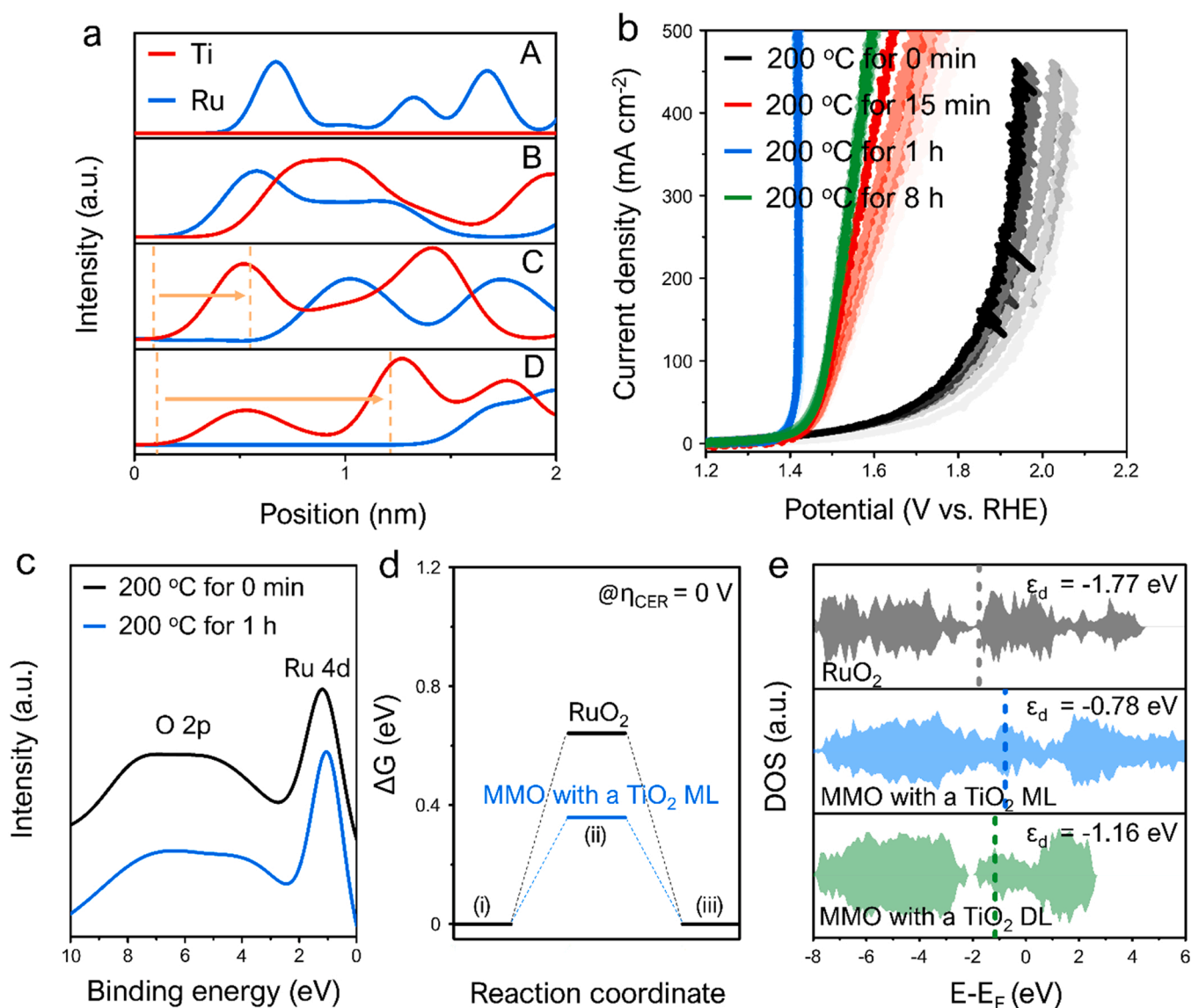


Fig. 4. (a) HAADF-STEM EDS line scan profiles of RNTO/Ti foam prepared with different annealing conditions: A) 200 °C for 0 min, B) 200 °C for 15 min, C) 200 °C for 1 h, and D) 200 °C for 8 h. The orange arrow corresponds to the TiO₂ shell thickness. (b) LSV curves measured at a scan rate of 10 mV s⁻¹ in 5.0 M NaCl electrolyte (pH = 2). (c) XPS valence band spectra of the RNTO/Ti foam showing the electronic structural change caused by annealing process. (d) Gibbs free energy diagram for CER on RuO₂ (110) surface and MMO (110) surface with TiO₂ mono-layer (mL) at zero overpotential ($\eta_{\text{CER}} = 0$ V). In the reaction coordinate, (i), (ii), and (iii) represent (i): 2Cl⁻, (ii): Cl⁻ + Cl⁻ + e⁻, and (iii): Cl₂ + e⁻. (e) Total density of state (DOS) and d-band center of RuO₂, MMO with a TiO₂ mono-layer, and MMO with a TiO₂ double-layer (DL).

and LSV results, it can be confirmed that the MMO formation and the thin TiO₂ shell are key origins for high electrocatalytic stability and activity.

Additionally, to understand the effect of the MMO formation and thin TiO₂ shell on electronic structure, intermediate binding strength, and free energy change of reaction, we measured the XPS valence band spectra and conducted density functional theory (DFT) calculation as shown in Fig. 4c–e. The computational models used for the DFT calculation are depicted in Fig. S21 and the detailed method is described in the Supplementary Material. It was identified from the XPS data that the d-band peak of Ru 4d shifts towards the Fermi level by the formation of MMO (Fig. 4c). Such an electronic structural change has been reported to improve the binding energies of adsorbates [74]. Indeed, it was also confirmed that the MMO surface model with a TiO₂ mono-layer significantly lowers the free energy barrier for CER (Fig. 4d), and strengthens the adsorption of a Cl intermediate (Fig. 4e and S21). However, as the TiO₂ gets thicker from mono-layer to double-layer, the d-band center

moves away from the Fermi level (Fig. 4e), resulting in weaker adsorption of the Cl intermediate. Therefore, the TiO₂ mono-layer as a passivation shell is considered to optimize the intermediate binding affinity. These calculation results agree well with experimental data and provide deeper understandings on the activity origin of RNTO/Ti foam catalysts.

In order to investigate the role of each element, we tried to prepare catalyst electrodes without Ru or Nb element with the similar procedure. The RNTO/Ti foam without Ru showed almost no electrocatalytic activity for CER (Fig. S22). In contrast the RNTO/Ti foam without Nb exhibited high electrocatalytic activity, but continuous decrease in the current density as the cycle number increased. According to our previous study, without Nb, the thermal diffusion of Ti atoms is not enough to completely form the MMO and the TiO₂ passivation layer [7]. Therefore, Ru element contributes to the CER activity while Nb enables durable CER performance because it acts as a promoter for thermal diffusion of Ti into RuO₂.

3.3. Charge transfer and mass transport analyses

According to the Butler–Volmer model, [45] it is known that the current density is regulated primarily by the charge-transfer process at a low overpotential region, while at high overpotentials that are sufficient to activate charge transfer, the mass transport process should be a rate-determining factor. Consequently, it can be postulated that the small overpotential of the RNTO/Ti foam at hundreds of mA cm^{-2} , compared to that of the RNTO/Ti foil, results from fast mass transport originating from the differences in electrode geometry.

To quantitatively evaluate the mass transport and charge transfer, Nyquist plots were measured using EIS analysis. It has been reported that the Nyquist plot helps calculate the R_{ct} at the catalyst-electrolyte interface, the R_{trms} across the catalyst layer, and the R_d controlled by the mass transport of the reactants for the analysis of various electrochemical reactions [75–79].

Fig. 4a shows the Nyquist plots of the RNTO/Ti foam, RNTO/Ti foil, and DSA obtained at an equilibrium potential of the CER in 5.0 M NaCl at 25 °C, 1.38 V vs. RHE, without magnetic stirring. All the curves show two semicircles, as identified in the enlarged view (Fig. S23). The equivalent circuit model used to fit the curves is shown in Fig. S24a. Because the reaction rate was slow at the equilibrium potential, large R_{ct} values were obtained (313, 1845, and 4619 Ω for the RNTO/Ti foam, RNTO/Ti foil, and DSA, respectively). The RNTO/Ti foam exhibited the smallest charge-transfer resistance at the catalyst-electrolyte interface. This trend explains why the RNTO/Ti foam showed the lowest onset potential in the LSV curve (Fig. 3a). Furthermore, the R_{trms} values of 0.21, 1.3, and 1.1 Ω were obtained for the RNTO/Ti foam, RNTO/Ti foil, and DSA, respectively (Fig. S23), which shows the different charge-transporting capabilities of the catalyst layer between the samples [75, 76, 79–83].

As the applied potential for EIS analysis was varied from 1.38 to 1.43 V vs. RHE, 50 mV higher than the equilibrium potential, the Nyquist plots showed considerable changes. As shown in Fig. 4b and S25, three semicircles were observed. According to previous studies, [80,84–86] the semicircles can be fitted with the equivalent circuit displayed in Fig. S24b, where a Nernst diffusion impedance is considered. At an applied potential of 1.43 V vs. RHE, the charge-transfer resistance decreases, and the semicircle shrinks significantly without overwhelming the semicircle assigned to the Nernst diffusion impedance.

The RNTO/Ti foam exhibited R_{trms} , R_{ct} , and R_d values of 0.7, 1.3, and 31.4 Ω , respectively, at 1.43 V vs. RHE without magnetic stirring, while the RNTO/Ti foil displayed larger resistances ($R_{trms} = 1.3 \Omega$, $R_{ct} = 8.9 \Omega$, $R_d = 142.8 \Omega$) under the same experimental conditions. These results indicate that the RNTO/Ti foam has better charge transfer and mass transport abilities than the RNTO/Ti foil. It is interesting to note that the diffusion resistance decreased as the magnetic stirring rate increased from 0 to 750 rpm (Fig. 4c and S25). This shows that stronger convection can reduce the diffusion resistance by supplying reactants at a faster rate [80]. Independent of the stirring speed, the RNTO/Ti foam (31.4, 9.7, 7.9, and 5.8 Ω at 0, 250, 500, and 750 rpm, respectively) always exhibited much faster mass transport than that of the RNTO/Ti foil (142.8, 19.1, 15.1, and 11.3 Ω at 0, 250, 500, and 750 rpm, respectively). Furthermore, assuming the Nernst diffusion layer of concentration gradient, diffusion layer thickness can be calculated by $\delta = \sqrt{3R_d C_d D_0}$, where C_d and D_0 ($2.03 \times 10^{-5} \text{ cm}^2 \text{ s}^{-1}$) correspond to the diffusion capacitance and the diffusion coefficient of Cl^- , respectively [80,86]. The diffusion layer thicknesses of the RNTO/Ti foam and RNTO/Ti foil were calculated to be 3.8 and 8.1 μm , respectively, at 1.43 V vs RHE under 500 rpm. These results confirm that the RNTO/Ti foam is outstanding for the high-rate CER controlled by mass transport.

To further investigate the effect of electrode geometry on mass transport, we measured the diffusion resistance (Fig. 4d) and LSV curves (Fig. 4e) with a sheet of tape attached to the back surface of the RNTO/Ti

foam sample. Attaching tape blocks the mass transport channels from the back surface and was expected to affect the electrocatalytic properties. Interestingly, it was observed that the differences between the R_d values of the RNTO/Ti foam and sample with tape attached increased as the stirring rate increased (Fig. 4d). The R_d values of the RNTO/Ti foam and RNTO/Ti foil decreased with increasing rpm from 0 rpm (31.4 and 35.2 Ω , respectively) to 250 rpm (9.7 and 15.2 Ω , respectively), 500 rpm (7.9 and 13.4 Ω , respectively), and 750 rpm (5.8 and 12.1 Ω , respectively). This result indicates that under convection conditions the back surface plays an important role as the primary mass transport channel. In the same context, in the LSV curves measured at 500 rpm (Fig. 4e), the two samples showed a large overpotential gap at high current densities (e.g., 182 mV at 400 mA cm^{-2}), although the onset potentials of these samples were very similar. Given that the ECSA values of the RNTO/Ti foam and blocked samples were similar (Fig. S26), these results confirmed that the small overpotential at the high current density achieved with the RNTO/Ti foam originated from the fast mass transport of the Cl^- reactants through the back surface, as schematically depicted in Fig. 4f. Similar to a gas diffusion electrode, a liquid diffusion electrode is provided with fresh reactants by liquid flowing through porous channels, whereas the CER mainly occurs near the front surface closer to the counter electrode, resulting in the formation of reactant concentration gradients.

3.4. Chlor-alkali electrolysis

To investigate the industrial applicability of the RNTO/Ti foam in the chlor-alkali process, we conducted a full-cell test using two RNTO/Ti foams as the cathode and anode (Fig. S27). Based on the practical electrolysis conditions that have been used, [87] saturated NaCl and 3.0 M NaOH/3.0 M NaCl solutions were adopted as the anolyte and catholyte, respectively, and heated to 90 °C. The chlor-alkali process proceeds with the HER at the cathode and CER at the anode, resulting in the net formation of NaOH, as shown in Fig. 5a. The Nafion membrane between the cathode and anode helped selectively pass cations (e.g., H^+ and Na^+ ions), thereby concentrating the catholyte with NaOH during the process.

Before the full-cell experiment, the electrocatalytic activity of the RNTO/Ti foam for the CER and HER was evaluated using LSV scans at a scan rate of 10 mV s^{-1} at 90 °C in saturated NaCl and 3.0 M NaOH/3.0 M NaCl solutions, respectively (Figs. 5b and 5c). For the CER, the current density increased sharply around the equilibrium potential ($E_{\text{CER}} = 1.58 \text{ V vs. RHE}$ at 90 °C in saturated NaCl) calculated based on the Nernst equation for the CER (see Experimental section in the ESI). The overpotential values applied were identified to be 39, 64, and 66 mV at 10, 100, and 500 mA cm^{-2} , respectively, which shows that the RNTO/Ti foam is still active for the CER even at higher temperatures and Cl^- concentrations. Moreover, the low Tafel slope of 37 mV dec^{-1} indicated that the process follows the Volmer–Heyrovsky mechanism (Fig. S28). The RNTO/Ti foam also exhibited fairly high HER activity in 3.0 M NaOH/3.0 M NaCl electrolyte at 90 °C, with 11 and 63 mV overpotentials at current densities of 10 and 100 mA cm^{-2} , respectively. Compared to other reported HER electrocatalysts, the RNTO/Ti foam showed competitive performance under experimental conditions for the chlor-alkali process (Table S3) [87–97]. Additionally, the Tafel slope of 33 mV dec^{-1} indicates that the HER process in the RNTO/Ti foam operated via the Volmer–Tafel mechanism, in which H–H coupling determines the rate of the HER (Fig. S29) [98].

Fig. 5d shows the LSV curve measured using a full cell at 90 °C with a stirring rate of 500 rpm. The RNTO/Ti foam exhibited low cell potentials of 1.67 and 1.83 V at 90 °C to obtain current densities of 10 and 100 mA cm^{-2} , respectively. Considering that the equilibrium cell potential of the chlor-alkali process at a temperature of 90 °C calculated using the Nernst equations of the CER and HER is 1.53 V (detailed information on the calculation is given in the ESI), the overpotentials for cell operation were as low as 140 and 300 mV at 10 and 100 mA cm^{-2} ,

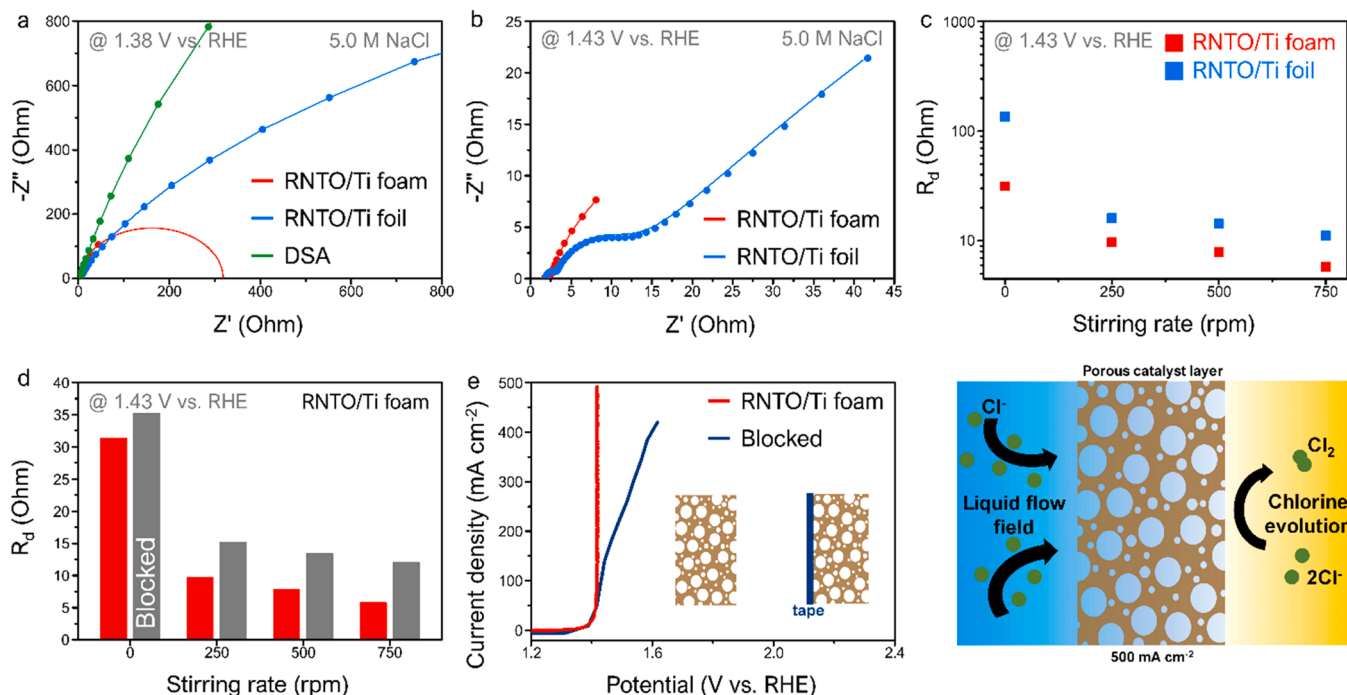


Fig. 5. (a) Nyquist plots of the fitting results for the RNTO/Ti foam, RNTO/Ti foil, and DSA measured at an equilibrium potential of the CER (1.38 V vs. RHE) in 5.0 M NaCl (pH = 2). (b) Nyquist plots of the fitting results for the RNTO/Ti foam and RNTO/Ti foil measured at 1.43 V vs. RHE (50 mV higher than equilibrium potential) in 5.0 M NaCl (pH = 2). (c) R_d of the RNTO/Ti foam and RNTO/Ti foil as a function of stirring rate. (d) R_d of the RNTO/Ti foam with or without blocking back surface. (e) LSV curve of the RNTO/Ti foam and blocked RNTO/Ti foam. (f) Schematic diagram of the RNTO/Ti foam acting as an LDE.

respectively, which are significantly lower than those reported (Table S4) [87,96]. Furthermore, the durability of the electrolytic cell was estimated using chronopotentiometry at 90 °C for 10 h at a current density of 100 mA cm^{-2} . As shown in Fig. 5e, the initial cell potential

was 1.84 V (cell overpotential was 310 mV), which was maintained during electrolysis with negligible fluctuations (less than $\pm 1.5\%$). These results show that the RNTO/Ti foam is a promising bifunctional electrode for the chlor-alkali process.

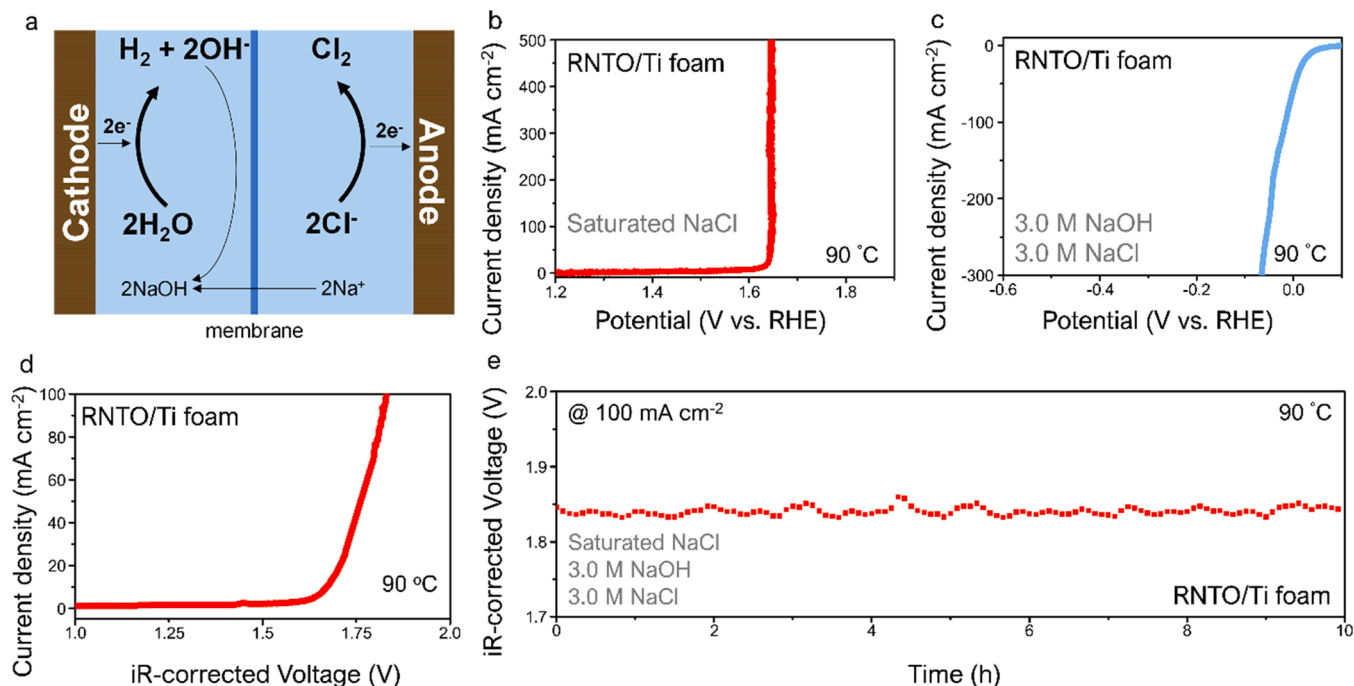


Fig. 6. (a) Illustration of the reaction steps in the chlor-alkali process. (b) CER LSV curve of the RNTO/Ti foam measured at a scan rate of 10 mV s^{-1} in saturated NaCl (pH = 6). (c) HER LSV curve of the RNTO/Ti foam measured in 3.0 M NaOH + 3.0 M NaCl (pH = 14.4). (d) Polarization curve of the RNTO/Ti foam for chlor-alkali electrolysis in two-electrode system. RNTO/Ti foam was used for both the anode and cathode. The anolyte was saturated NaCl (pH = 6) and the catholyte was 3.0 M NaOH + 3.0 M NaCl (pH = 14.4). (e) Chronopotentiometry curve of the RNTO/Ti foam in a simulated chlor-alkali environment measured at 100 mA cm^{-2} for 10 h. The electrolyte was continuously supplied by using a flow cell.

4. Conclusion

In summary, we demonstrated that porous, conductive Ti foam scaffolds decorated with core/shell structured nanoparticles composed of a Ru–Ti–Nb–O core and titania passivation layer enabled near-zero polarization behavior independent of current density as an anode for the CER. Specifically, the RNTiO/Ti foam showed an almost zero overpotential of 9 mV with an exceptional FE of 99.1% at 10 mA cm⁻² for the CER, as well as exhibiting a very low overpotential of 44 mV even at a high current density of 500 mA cm⁻² with a high FE of 86.1%. These CER results represent record-high values compared to those of reported studies. The zero overpotential at a low current density is attributed to fast charge-transfer kinetics, originating from the formation of 2 nm sized efficient and durable MMO active sites, as well as a high electrode surface area, while fast mass transport by liquid diffusion through the back surface of the Ti foam allowed for a low overpotential even at a current density of hundreds of mA cm⁻². Furthermore, under the practical conditions of the chlor-alkali process, the RNTiO/Ti foam exhibited a stable and efficient electrocatalytic performance as a bifunctional electrode for cell operation. The cell potential of 1.84 V (equivalent to 310 mV of overpotential) remained stable at 100 mA cm⁻² at 90 °C for 10 h. Consequently, the outstanding performance of the RNTiO/Ti foam in terms of overpotential, Faradaic efficiency, and stability offers great promise in the practical implementation of a liquid-diffusion electrode as a next-generation DSA for the chlor-alkali industry. (Fig. 6).

CRediT authorship contribution statement

Hyun Woo Lim: Conceptualization, Investigation, Writing – original draft, Writing – review & editing. **Jae Hyun Park:** Investigation, Resources, Formal analysis. **Bingyi Yan:** Investigation, Formal analysis. **Jin Young Kim:** Conceptualization, Supervision, Validation, Writing – review & editing. **Chan Woo Lee:** Conceptualization, Supervision, Project administration, Validation, Writing – original draft, Writing – review & editing.

Declaration of Competing Interest

The authors declare that they have no known competing financial interests or personal relationships that could have appeared to influence the work reported in this paper.

Data Availability

Data will be made available on request.

Acknowledgements

This work was supported by the National Research Foundation of Korea (NRF) Grant funded by the Korean Government (MSTI) (NRF-2020R1C1C1010963, NRF-2022R1A4A1019296, NRF-2022M3H4A4097525). This work was also supported by the National Research Foundation of Korea (NRF) funded by the Creative Materials Discovery Program, South Korea (No. 2017M3D1A1039377). This work was supported by the KIST Institutional Program (Project No. 2V09300-22-055). This work was supported by National Research and Development Program through the National Research Foundation of Korea (NRF) funded by Ministry of Science and ICT (No. 2021M3H4A1A03057403).

Appendix A. Supporting information

Supplementary data associated with this article can be found in the online version at doi:10.1016/j.apcatb.2022.122095.

References

- [1] H. Wang, Z. Han, Y. Zhou, X. Liu, D. Zeng, W. Wang, D. Sarker, L. Zhang, W. Wang, Efficient photocatalytic chlorine production on bismuth oxychloride in chloride solution, *Appl. Catal. B Environ.* 297 (2021), 120436, <https://doi.org/10.1016/j.apcatb.2021.120436>.
- [2] T. Cui, J. Chi, J. Zhu, X. Sun, J. Lai, Z. Li, L. Wang, Tuning the size and chemisorption of FeP4 by trace Ru doping for hydrazine-assisted hydrogen evolution in seawater at large-current-density, *Appl. Catal. B Environ.* 319 (2022), 121950, <https://doi.org/10.1016/j.apcatb.2022.121950>.
- [3] World Chlorine Council, The World Chlorine Council and Sustainable Development, 2002. (<https://www.worldchlorine.org/wp-content/themes/brickthemewp/pdfs/report.pdf>).
- [4] E. Worrel, D. Philipsen, D. Einstein, N. Martin, Energy Use and Energy Intensity of the U.S. Chemical Industry, Lawrence Berkeley Natl. Lab. LBNL-44314 (2000) 34. https://www.energystar.gov/ia/business/industry/industrial_LBNL-44314.pdf.
- [5] X. Wang, H. Teichgraber, A. Palazoglu, N.H. El-Farra, An economic receding horizon optimization approach for energy management in the chlor-alkali process with hybrid renewable energy generation, *J. Process Control.* 24 (2014) 1318–1327, <https://doi.org/10.1016/j.jprocont.2014.04.017>.
- [6] G. van Oortmerssen, Sustainable Progress, 2017. (https://worldchlorine.org/wp-content/uploads/2018/10/WCC_Sustainable-Progress_Version-3-2017.pdf).
- [7] H.W. Lim, D.K. Cho, J.H. Park, S.G. Ji, Y.J. Ahn, J.Y. Kim, C.W. Lee, Rational design of dimensionally stable anodes for active chlorine generation, *ACS Catal.* 11 (2021) 12423–12432, <https://doi.org/10.1021/acscatal.1c03653>.
- [8] H. Ha, K. Jin, S. Park, K.-G. Lee, K. Hee Cho, H. Seo, H.-Y. Ahn, Y. Ho Lee, K. Tae Nam, Highly selective active chlorine generation electrocatalyzed by Co₃O₄ nanoparticles: mechanistic investigation through in situ electrokinetic and spectroscopic, *Anal. J. Phys. Chem. Lett.* 10 (2019) 1226–1233, <https://doi.org/10.1021/acs.jpcl.9b00547>.
- [9] E. Tsolaki, E. Diamadopoulos, Technologies for ballast water treatment: a review, *J. Chem. Technol. Biotechnol.* 85 (2010) 19–32, <https://doi.org/10.1002/jctb.2276>.
- [10] T.V. Mommaraaju, T.F. O'Brien, Brine Electrolysis, New York, 2007. (<http://electrochem.cwrw.edu/encycl/art-b01-brine.htm>) ed.
- [11] World Chlorine Council, Products of the Chlorine Tree, World Chlorine Council. (https://worldchlorine.org/wp-content/uploads/2014/03/Chlorine-Product-Tree_012017.pdf).
- [12] J. Pérez-Ramírez, C. Mondelli, T. Schmidt, O.F.K. Schlüter, A. Wolf, L. Mleczko, T. Dreier, Sustainable chlorine recycling via catalysed HCl oxidation: from fundamentals to implementation, *Energy Environ. Sci.* 4 (2011) 4786–4799, <https://doi.org/10.1039/c1ee02190g>.
- [13] J. Fauvarque, The chlorine industry, *Pure Appl. Chem.* 68 (1996) 1713–1720, <https://doi.org/10.1351/pac199668091713>.
- [14] J. Jung, S. Postels, A. Bardow, Cleaner chlorine production using oxygen depolarized cathodes? A life cycle assessment, *J. Clean. Prod.* 80 (2014) 46–56, <https://doi.org/10.1016/j.jclepro.2014.05.086>.
- [15] M. Rabbani, I. Dincer, G.F. Naterer, Experimental investigation of processing parameters and effects on chloralkali products in an electrolysis based chloralkali reactor, *Chem. Eng. Process. Process. Intensif.* 82 (2014) 9–18, <https://doi.org/10.1016/j.cep.2014.04.007>.
- [16] R.K.B. Karlsson, A. Cornell, Selectivity between oxygen and chlorine evolution in the chlor-alkali and chlorate processes, *Chem. Rev.* 116 (2016) 2982–3028, <https://doi.org/10.1021/acs.chemrev.5b00389>.
- [17] M. Hou, L. Chen, Z. Guo, X. Dong, Y. Wang, Y. Xia, A clean and membrane-free chlor-alkali process with decoupled Cl₂ and H₂/NaOH production, *Nat. Commun.* 9 (2018) 438, <https://doi.org/10.1038/s41467-018-02877-x>.
- [18] S. Lakshmanan, T. Murugesan, The chlor-alkali process: work in progress, *Clean. Technol. Environ. Policy* 16 (2014) 225–234, <https://doi.org/10.1007/s10098-013-0630-6>.
- [19] A. Kumar, F. Du, J.H. Lienhard, Caustic soda production, energy efficiency, and electrolyzers, *ACS Energy Lett.* 6 (2021) 3563–3566, <https://doi.org/10.1021/acsenenergylett.1c01827>.
- [20] World Chlorine Council, Chlorine's important co-product: caustic soda, 2002. (http://www.worldchlorine.org/wp-content/themes/brickthemewp/pdfs/caustic_soda.pdf).
- [21] P. Examiner, B.F. Bell, (12) United States Patent, United States Pat. 1 (2002).
- [22] C. Zhang, W. Zhang, N.E. Drewett, X. Wang, S.J. Yoo, H. Wang, T. Deng, J.G. Kim, H. Chen, K. Huang, S. Feng, W. Zheng, Integrating catalysis of methane decomposition and electrocatalytic hydrogen evolution with Ni/CeO₂ for improved hydrogen production efficiency, *ChemSusChem* 12 (2019) 1000–1010, <https://doi.org/10.1002/cssc.201802618>.
- [23] S. Trasatti, G. Buzzanca, Ruthenium dioxide: a new interesting electrode material. Solid state structure and electrochemical behaviour, *J. Electroanal. Chem. Interfacial Electrochem* 29 (1971) A1–A5, [https://doi.org/10.1016/S0022-0728\(71\)80111-0](https://doi.org/10.1016/S0022-0728(71)80111-0).
- [24] V. Krstić, B. Pešovski, Reviews the research on some dimensionally stable anodes (DSA) based on titanium, *Hydrometallurgy* 185 (2019) 71–75, <https://doi.org/10.1016/j.hydromet.2019.01.018>.
- [25] H. Over, Surface chemistry of ruthenium dioxide in heterogeneous catalysis and electrocatalysis: from fundamental to applied research, *Chem. Rev.* 112 (2012) 3356–3426, <https://doi.org/10.1021/cr200247n>.
- [26] N. Menzel, E. Ortel, K. Mette, R. Kraehnert, P. Strasser, Dimensionally stable Ru/Ir/TiO₂-anodes with tailored mesoporosity for efficient electrochemical chlorine evolution, *ACS Catal.* 3 (2013) 1324–1333, <https://doi.org/10.1021/cs4000238>.

- [27] C. Comninellis, G.P. Vercesi, Problems in DSA | coating deposition by thermal decomposition, *J. Appl. Electrochem* 21 (1991) 136–142, <https://doi.org/10.1007/BF01464294>.
- [28] S. Trasatti, *Conductive Metal Oxides*, Bd. A., Elsevier, Amsterdam, 1980.
- [29] T. S. Electrochemical: understanding the success of DSA®, *Electrochim. Acta* 45 (2000) 2377–2385, (<http://www.sciencedirect.com/science/article/pii/S0013468600003388>).
- [30] S. Trasatti, Physical electrochemistry of ceramic oxides, *Electrochim. Acta* 36 (1991) 225–241, [https://doi.org/10.1016/0013-4686\(91\)85244-2](https://doi.org/10.1016/0013-4686(91)85244-2).
- [31] G. Lodit, E. Sivieri, S. Trasatti, Ruthenium dioxide-based film electrodes, *J. Appl. Electrochem* 8 (1978) 135–143, <https://doi.org/10.1007/BF00617671>.
- [32] K.M. Glassford, J.R. Chelikowsky, Electronic and structural properties of RuO₂, *Phys. Rev. B* 47 (1993) 1732–1741, <https://doi.org/10.1103/PhysRevB.47.1732>.
- [33] E. Dy, R. Hui, J. Zhang, Z.S. Liu, Z. Shi, Electronic conductivity and stability of doped titania (Ti_{1-x}M_xO₂, M = Nb, Ru, and Ta)- a density functional Theory-Based comparison, *J. Phys. Chem. C* 114 (2010) 13162–13167, <https://doi.org/10.1021/jp100826g>.
- [34] Y. Wang, Y. Liu, D. Wiley, S. Zhao, Z. Tang, Recent advances in electrocatalytic chlorine oxidation for chlorine gas production, *J. Mater. Chem. A* (2021), <https://doi.org/10.1039/D1TA02745J>.
- [35] J. Huang, M. Hou, J. Wang, X. Teng, Y. Niu, M. Xu, Z. Chen, RuO₂ nanoparticles decorate belt-like anatase TiO₂ for highly efficient chlorine evolution, *Electrochim. Acta* 339 (2020), 135878, <https://doi.org/10.1016/j.electacta.2020.135878>.
- [36] M. Jiang, H. Wang, Y. Li, H. Zhang, G. Zhang, Z. Lu, X. Sun, L. Jiang, Superaerophobic RuO₂-based nanostructured electrode for high-performance chlorine evolution reaction, *Small* 13 (2017) 1–8, <https://doi.org/10.1002/sml.201602240>.
- [37] K. Xiong, Z. Deng, L. Li, S. Chen, M. Xia, L. Zhang, X. Qi, W. Ding, S. Tan, Z. Wei, Sn and Sb co-doped RuTi oxides supported on TiO₂ nanotubes anode for selectivity toward electrocatalytic chlorine evolution, *J. Appl. Electrochem.* 43 (2013) 847–854, <https://doi.org/10.1007/s10800-013-0570-1>.
- [38] K. Xiong, L. Peng, Y. Wang, L. Liu, Z. Deng, L. Li, Z. Wei, In situ growth of RuO₂-TiO₂ catalyst with flower-like morphologies on the Ti substrate as a binder-free integrated anode for chlorine evolution, *J. Appl. Electrochem.* 46 (2016) 841–849, <https://doi.org/10.1007/s10800-016-0934-4>.
- [39] W. Cheng, Y. Liu, L. Wu, R. Chen, J. Wang, S. Chang, F. Ma, Y. Li, H. Ni, RuO₂/IrO₂ nanoparticles decorated TiO₂ nanotube arrays for improved activity towards chlorine evolution reaction, *Catal. Today* 400–401 (2022) 26–34, <https://doi.org/10.1016/j.cattod.2022.04.004>.
- [40] K.S. Exner, J. Anton, T. Jacob, H. Over, Controlling selectivity in the chlorine evolution reaction over RuO₂-based catalysts, *Angew. Chem. Int. Ed.* 126 (2014) 11212–11215, <https://doi.org/10.1002/anie.201406112>.
- [41] I. Sohrabnejad-Eskan, A. Goryachev, K.S. Exner, L.A. Kibler, E.J.M. Hensen, J. P. Hofmann, H. Over, Temperature-dependent kinetic studies of the chlorine evolution reaction over RuO₂(110) model electrodes, *ACS Catal.* 7 (2017) 2403–2411, <https://doi.org/10.1021/acscatal.6b03415>.
- [42] K.S. Exner, H. Over, Kinetics of electrocatalytic reactions from first-principles: a critical comparison with the Ab initio thermodynamics approach, *Acc. Chem. Res.* 50 (2017) 1240–1247, <https://doi.org/10.1021/acs.accounts.7b00077>.
- [43] K.S. Exner, Overpotential-dependent volcano plots to assess activity trends in the competing chlorine and oxygen evolution reactions, *ChemElectroChem* 7 (2020) 1448–1455, <https://doi.org/10.1002/celec.202000120>.
- [44] T. Lim, J.H. Kim, J. Kim, S. Baek, J. Shin, Y. Jeong, K.-S. Lee, K.S. Exner, S.H. Joo, General efficacy of atomically dispersed Pt catalysts for the chlorine evolution reaction: potential-dependent switching of the kinetics and mechanism, *ACS Catal.* 11 (2021) 12232–12246, <https://doi.org/10.1021/acscatal.1c03893>.
- [45] A.J. Bard, L.R. Faulkner, *Electrochemical Methods: Fundamentals and Applications*, second ed., Wiley, New York, 2002 <https://doi.org/10.1023/S:1021637209564>.
- [46] M. Iurlo, M. Marcaccio, F. Paolucci, *Modern Electrochemistry* 2A, Springer, Boston, 2002, <https://doi.org/10.1002/9783527629930.ch3>.
- [47] D. Wakerley, S. Lemaire, J. Wicks, A. Clemens, J. Feaster, D. Corral, S.A. Jaffer, A. Sarkar, M. Fontecave, E.B. Duoss, S. Baker, E.H. Sargent, T.F. Jaramillo, C. Hahn, Gas diffusion electrodes, reactor designs and key metrics of low-temperature CO₂ electrolyzers, *Nat. Energy* 7 (2022) 130–143, <https://doi.org/10.1038/s41560-021-00973-9>.
- [48] E. Guerrini, V. Consonni, S. Trasatti, Surface and electrocatalytic properties of well-defined and vicinal RuO₂ single crystal faces, *J. Solid State Electrochem.* 9 (2005) 320–329, <https://doi.org/10.1007/s10008-004-0602-1>.
- [49] S.G. Bratsch, Standard electrode potentials and temperature coefficients in water at 298.15 K, *J. Phys. Chem. Ref. Data* 18 (1989) 1–21, <https://doi.org/10.1063/1.555839>.
- [50] S.E. Heo, H.W. Lim, D.K. Cho, I.J. Park, H. Kim, C.W. Lee, S.H. Ahn, J.Y. Kim, Anomalous potential dependence of conducting property in black titania nanotube arrays for electrocatalytic chlorine evolution, *J. Catal.* 381 (2020) 462–467, <https://doi.org/10.1016/j.jcat.2019.11.030>.
- [51] D.L. Harp, Current technology of chlorine analysis for water and wastewater. Technical Information Series, Hach Company Inc., Colorado, 2002.
- [52] C. Wei, S. Sun, D. Mandler, X. Wang, S.Z. Qiao, Z.J. Xu, Approaches for measuring the surface areas of metal oxide electrocatalysts for determining their intrinsic electrocatalytic activity, *Chem. Soc. Rev.* 48 (2019) 2518–2534, <https://doi.org/10.1039/c8cs00848e>.
- [53] W. Choi, H.C. Shin, J.M. Kim, J.Y. Choi, W.S. Yoon, Modeling and applications of electrochemical impedance spectroscopy (Eis) for lithium-ion batteries, *J. Electrochem. Sci. Technol.* 11 (2020) 1–13, <https://doi.org/10.33961/jecst.2019.00528>.
- [54] U. Krewer, F. Röder, E. Harinath, R.D. Braatz, B. Bedürftig, R. Findeisen, Review—dynamic models of Li-Ion batteries for diagnosis and operation: a review and perspective, *J. Electrochem. Soc.* 165 (2018) A3656–A3673, <https://doi.org/10.1149/2.1061814jes>.
- [55] O.A. Petrii, *Encyclopedia of Electrochemical Power Sources*, Elsevier, New York, 2009, (<http://www.sciencedirect.com/science/article/pii/B9780444527455008686>).
- [56] H. Choi, H. Park, J.H. Um, W.S. Yoon, H. Choe, Processing and characterization of titanium dioxide grown on titanium foam for potential use as Li-ion electrode, *Appl. Surf. Sci.* 411 (2017) 363–367, <https://doi.org/10.1016/j.apsusc.2017.03.122>.
- [57] J. Balcerzak, W. Redzyna, J. Tyczkowski, In-situ XPS analysis of oxidized and reduced plasma deposited ruthenium-based thin catalytic films, *Appl. Surf. Sci.* 426 (2017) 852–855, <https://doi.org/10.1016/j.apsusc.2017.07.248>.
- [58] J.F. Moulder, W.F. Stickle, P.E. Sobol, K.D. Bomben, *Handbook of X-ray photoelectron spectroscopy: a reference book of standard spectra for identification and interpretation of XPS data*, Perkin Elmer Corp. (1992) <https://www.cnyun.unam.mx/~wencil/XPS/MANXPS.pdf>.
- [59] M. Fehse, S. Cavaliere, P.E. Lippens, I. Savych, A. Iadecola, L. Monconduit, D.J. Jones, F. Fischer, C. Tessier, L. Stievano, D. De Recherche, B.A. Daney, Nb-Doped TiO₂ Nano fi bers for Lithium Ion Batteries, (2013).
- [60] S. Yang, Z. Han, X. Pan, Z. Yan, J. Yu, Nitrogen oxide removal using seawater electrolysis in an undivided cell for ocean-going vessels, *RSC Adv.* 6 (2016) 114623–114631, <https://doi.org/10.1039/c6ra24537d>.
- [61] D.-Y. Kuo, H. Paik, J.N. Nelson, K.M. Shen, D.G. Schlom, J. Suntivich, Chlorine evolution reaction electrocatalysis on RuO₂ (110) and IrO₂ (110) grown using molecular-beam epitaxy, *J. Chem. Phys.* 150 (2019) 41726, <https://doi.org/10.1063/1.5051429>.
- [62] K.S. Exner, J. Anton, T. Jacob, H. Over, Chlorine evolution reaction on RuO₂ (110): Ab initio atomistic thermodynamics study - pourbaix diagrams, *Electrochim. Acta* 120 (2014) 460–466, <https://doi.org/10.1016/j.electacta.2013.11.027>.
- [63] K.S. Exner, J. Anton, T. Jacob, H. Over, Full kinetics from first principles of the chlorine evolution reaction over a RuO₂(110) model electrode, *Angew. Chem. Int. Ed.* 55 (2016) 7501–7504, <https://doi.org/10.1002/anie.201511804>.
- [64] H.A. Hansen, I.C. Man, F. Studt, F. Abild-Pedersen, T. Bligaard, J. Rossmeisl, Electrochemical chlorine evolution at rutile oxide (110) surfaces, *Phys. Chem. Chem. Phys.* 12 (2010) 283–290, <https://doi.org/10.1039/b917459a>.
- [65] M. Vuković, Rotating ring-disc electrode study of the enhanced oxygen evolution on an activated ruthenium electrode, *J. Chem. Soc. Faraday Trans.* 86 (1990) 3743–3746, <https://doi.org/10.1039/FT9908603743>.
- [66] C. Roy, R.R. Rao, K.A. Stoerzinger, J. Hwang, J. Rossmeisl, I. Chorkendorff, Y. Shao-Horn, I.E.L. Stephens, Trends in activity and dissolution on RuO₂ under oxygen evolution conditions: particles versus well-defined extended surfaces, *ACS Energy Lett.* 3 (2018) 2045–2051, <https://doi.org/10.1021/acsenenerglett.8b01178>.
- [67] I.A. Moreno-Hernandez, B.S. Brunschwig, N.S. Lewis, Crystalline nickel, cobalt, and manganese antimonates as electrocatalysts for the chlorine evolution reaction, *Energy Environ. Sci.* 12 (2019) 1241–1248, <https://doi.org/10.1039/c8ee03676d>.
- [68] R. Chen, V. Trieu, A.R. Zeradjanin, H. Natter, D. Teschner, J.J. Kintrup, A. Bulan, W. Schuhmann, R. Hempelmann, Microstructural impact of anodic coatings on the electrochemical chlorine evolution reaction, *Phys. Chem. Chem. Phys.* 14 (2012) 7392–7399, <https://doi.org/10.1039/c2cp41163f>.
- [69] F. Zhang, X. Gu, S. Zheng, H. Yuan, J. Li, X. Wang, Highly catalytic flexible RuO₂ on carbon fiber cloth network for boosting chlorine evolution reaction, *Electrochim. Acta* 307 (2019) 385–392, <https://doi.org/10.1016/j.electacta.2019.03.187>.
- [70] C.E. Finke, S.T. Omelchenko, J.T. Jasper, M.F. Lichterman, C.G. Read, N.S. Lewis, M.R. Hoffmann, Enhancing the activity of oxygen-evolution and chlorine-evolution electrocatalysts by atomic layer deposition of TiO₂, *Energy Environ. Sci.* 12 (2019) 358–365, <https://doi.org/10.1039/c8ee02351d>.
- [71] X. Zhu, P. Wang, Z. Wang, Y. Liu, Z. Zheng, Q. Zhang, X. Zhang, Y. Dai, M. H. Wangbo, B. Huang, Co₃O₄ nanobelt arrays assembled with ultrathin nanosheets as highly efficient and stable electrocatalysts for the chlorine evolution reaction, *J. Mater. Chem. A* 6 (2018) 12718–12723, <https://doi.org/10.1039/c8ta03689f>.
- [72] T. Lim, G.Y. Jung, J.H. Kim, S.O. Park, J. Park, Y.T. Kim, S.J. Kang, H.Y. Jeong, S. K. Kwak, S.H. Joo, Atomically dispersed Pt–N₄ sites as efficient and selective electrocatalysts for the chlorine evolution reaction, *Nat. Commun.* 11 (2020) 412, <https://doi.org/10.1038/s41467-019-14272-1>.
- [73] Y. Wang, Y. Xue, C.Y. Zhang Wang, C. Zhang, Rational surface and interfacial engineering of IrO₂/TiO₂ nanosheet arrays toward high-performance chlorine evolution electrocatalysis and practical environmental remediation, *Small* 17 (2021), 2006587, <https://doi.org/10.1002/sml.202006587>.
- [74] J.F. Godínez-Salomón, F. Ospina-Acevedo, L.A. Albiter, K.O. Bailey, Z.G. Naymik, R. Mendoza-Cruz, P.B. Balbuena, C.P. Rhodes, Titanium substitution effects on the structure, activity, and stability of nanoscale ruthenium oxide oxygen evolution electrocatalysts: experimental and computational study, *ACS Appl. Nano Mater.* (2022), <https://doi.org/10.1021/acsnanm.2c02760>.
- [75] H. Seo, K. Jin, S. Park, K.H. Cho, H. Ha, K.G. Lee, Y.H. Lee, D.T. Nguyen, H. Randriamahazaka, J.S. Lee, K.T. Nam, Mechanistic investigation with kinetic parameters on water oxidation catalyzed by manganese oxide nanoparticle film, *ACS Sustain. Chem. Eng.* 7 (2019) 10595–10604, <https://doi.org/10.1021/acssuschemeng.9b01159>.
- [76] D.V. Morales, C.N. Astudillo, V. Anastasoie, B. Dautreppe, B.F. Urbano, B.L. Rivas, C. Gondran, D. Aldakov, B. Chovelon, D. André, J.L. Putaux, C. Lancelon-Pin, S. Sirach, E.M. Ungureanu, C. Costentin, M.N. Collomb, J. Fortage, A cobalt oxide-

- polypyrrole nanocomposite as an efficient and stable electrode material for electrocatalytic water oxidation, *Sustain. Energy Fuels* 5 (2021) 4710–4723, <https://doi.org/10.1039/d1se00363a>.
- [77] G. Li, L. Anderson, Y. Chen, M. Pan, P.Y. Abel Chuang, New insights into evaluating catalyst activity and stability for oxygen evolution reactions in alkaline media, *Sustain. Energy Fuels* 2 (2018) 237–251, <https://doi.org/10.1039/c7se00337d>.
- [78] Y. Meng, W. Song, H. Huang, Z. Ren, S.Y. Chen, S.L. Suib, Structure-property relationship of bifunctional MnO₂ nanostructures: Highly efficient, ultra-stable electrochemical water oxidation and oxygen reduction reaction catalysts identified in alkaline media, *J. Am. Chem. Soc.* 136 (2014) 11452–11464, <https://doi.org/10.1021/ja505186m>.
- [79] J.S. Kim, S.S. Shin, H.S. Han, L.S. Oh, D.H. Kim, J.H. Kim, K.S. Hong, J.Y. Kim, 1-D structured flexible supercapacitor electrodes with prominent electronic/ionic transport capabilities, *ACS Appl. Mater. Interfaces* 6 (2014) 268–274, <https://doi.org/10.1021/am404132j>.
- [80] Z. Xing, X. Hu, X. Feng, Tuning the microenvironment in gas-diffusion electrodes enables high-rate CO₂ electrolysis to formate, *ACS Energy Lett.* 6 (2021) 1694–1702, <https://doi.org/10.1021/acsenenergylett.1c00612>.
- [81] F. El-Taib Heakal, W.R. Abd-Ellatif, N.S. Tantawy, A.A. Taha, Impact of pH and temperature on the electrochemical and semiconducting properties of zinc in alkaline buffer media, *RSC Adv.* 8 (2018) 3816–3827, <https://doi.org/10.1039/c7ra12723e>.
- [82] C.Q. Ye, R.G. Hu, S.G. Dong, X.J. Zhang, R.Q. Hou, R.G. Du, C.J. Lin, J.S. Pan, EIS analysis on chloride-induced corrosion behavior of reinforcement steel in simulated carbonated concrete pore solutions, *J. Electroanal. Chem.* 688 (2013) 275–281, <https://doi.org/10.1016/j.jelechem.2012.09.012>.
- [83] Q. Yang, Y. Cui, Q. Li, J. Cai, D. Wang, L. Feng, Nanosheet-derived ultrafine CoRuO_x@NC nanoparticles with a core@shell structure as bifunctional electrocatalysts for electrochemical water splitting with high current density or low power input, *ACS Sustain. Chem. Eng.* 8 (2020) 12089–12099, <https://doi.org/10.1021/acssuschemeng.0c03410>.
- [84] W. Kwon, J.M. Kim, S.W. Rhee, A new equivalent circuit model for porous carbon electrodes in charge transfer reaction of iodide/triiodide redox couples, *Electrochim. Acta* 68 (2012) 110–113, <https://doi.org/10.1016/j.electacta.2012.02.056>.
- [85] J. Bisquert, G. Garcia-Belmonte, F. Fabregat-Santiago, P.R. Bueno, Theoretical models for ac impedance of finite diffusion layers exhibiting low frequency dispersion, *J. Electroanal. Chem.* 475 (1999) 152–163, [https://doi.org/10.1016/S0022-0728\(99\)00346-0](https://doi.org/10.1016/S0022-0728(99)00346-0).
- [86] W. Zhang, J. Ma, P. Wang, Z. Wang, F. Shi, H. Liu, Investigations on the interfacial capacitance and the diffusion boundary layer thickness of ion exchange membrane using electrochemical impedance spectroscopy, *J. Memb. Sci.* 502 (2016) 37–47, <https://doi.org/10.1016/j.memsci.2015.12.007>.
- [87] L.-N. Zhang, Z.-L. Lang, Y.-H. Wang, H.-Q. Tan, H.-Y. Zang, Z.-H. Kang, Y.-G. Li, Cable-like Ru/WNO@C nanowires for simultaneous high-efficiency hydrogen evolution and low-energy consumption chlor-alkali electrolysis, *Energy Environ. Sci.* 12 (2019) 2569, <https://doi.org/10.1039/c9ee01647c>.
- [88] R. Solmaz, G. Kardaş, Fabrication and characterization of NiCoZn–M (M: Ag, Pd and Pt) electrocatalysts as cathode materials for electrochemical hydrogen production, *Int. J. Hydrog. Energy* 36 (2011) 12079–12087, <https://doi.org/10.1016/j.ijhydene.2011.06.101>.
- [89] C.I. Müller, T. Rauscher, A. Schmidt, T. Schubert, T. Weißgärber, B. Kieback, L. Röntzsch, Electrochemical investigations on amorphous Fe-base alloys for alkaline water electrolysis, *Int. J. Hydrog. Energy* 39 (2014) 8926–8937, <https://doi.org/10.1016/j.ijhydene.2014.03.151>.
- [90] A.O. Yüce, A. Döner, G. Kardaş, NiMn composite electrodes as cathode material for hydrogen evolution reaction in alkaline solution, *Int. J. Hydrog. Energy* 38 (2013) 4466–4473, <https://doi.org/10.1016/j.ijhydene.2013.01.160>.
- [91] S.M.A. Shibli, J.N. Sebeelamol, Development of Fe₂O₃–TiO₂ mixed oxide incorporated Ni–P coating for electrocatalytic hydrogen evolution reaction, *Int. J. Hydrog. Energy* 38 (2013) 2271–2282, <https://doi.org/10.1016/j.ijhydene.2012.12.009>.
- [92] L.J. Song, H.M. Meng, Effect of carbon content on Ni–Fe–C electrodes for hydrogen evolution reaction in seawater, *Int. J. Hydrog. Energy* 35 (2010) 10060–10066, <https://doi.org/10.1016/j.ijhydene.2010.08.003>.
- [93] F. Rosalbino, D. Macciò, A. Saccone, G. Scavino, Study of Co–W crystalline alloys as hydrogen electrodes in alkaline water electrolysis, *Int. J. Hydrog. Energy* 39 (2014) 12448–12456, <https://doi.org/10.1016/j.ijhydene.2014.06.082>.
- [94] D.M.F. Santos, C.A.C. Sequeira, D. Macciò, A. Saccone, J.L. Figueiredo, Platinum–rare earth electrodes for hydrogen evolution in alkaline water electrolysis, *Int. J. Hydrog. Energy* 38 (2013) 3137–3145, <https://doi.org/10.1016/j.ijhydene.2012.12.102>.
- [95] L. Mihailov, T. Spassov, M. Bojinov, Effect of microstructure on the electrocatalytic activity for hydrogen evolution of amorphous and nanocrystalline Zr–Ni alloys, *Int. J. Hydrog. Energy* 37 (2012) 10499–10506, <https://doi.org/10.1016/j.ijhydene.2012.04.042>.
- [96] A. Salah, L. Zhang, H. Tan, F. Yu, Z. Lang, N. Al-Ansi, Y. Li, Advanced Ru/Ni/WC@NPC multi-interfacial electrocatalyst for efficient sustainable hydrogen and chlor-alkali Co-production, *Adv. Energy Mater.* 12 (2022), 2200332, <https://doi.org/10.1002/aenm.202200332>.
- [97] L.N. Zhang, R. Li, H.Y. Zang, H.Q. Tan, Z.H. Kang, Y.H. Wang, Y.G. Li, Advanced hydrogen evolution electrocatalysts promising sustainable hydrogen and chlor-alkali co-production, *Energy Environ. Sci.* 14 (2021) 6191–6210, <https://doi.org/10.1039/d1ee02798k>.
- [98] H. Wang, Z. Han, Y. Zhou, X. Liu, D. Zeng, W. Wang, D. Sarker, L. Zhang, W. Wang, Efficient photocatalytic chlorine production on bismuth oxychloride in chloride solution, *Appl. Catal. B Environ.* 297 (2021), 120436, <https://doi.org/10.1016/j.apcatb.2021.120436>.